Plasmon-Driven Chemistry in Ferri-/Ferrocyanide Gold Nanoparticle Oligomers: A SERS Study

*Yue Qi, Vitor Brasiliense, Tyler W. Ueltschi, Ji Eun Park, Michael R. Wasielewski, * George C. Schatz, * and Richard P. Van Duyne†*

Department of Chemistry, Northwestern University, 2145 Sheridan Road, Evanston, Illinois 60208, United States

KEYWORDS plasmon-driven chemistry, surface-enhanced Raman spectroscopy, hot-hole chemistry, localized surface plasmon resonance

ABSTRACT: The plasmon-driven chemistry of ferri-/ferrocyanide ions inside surface-enhanced Raman spectroscopy (SERS) active hot spots associated with gold nanoparticle oligomers is studied with continuous wave (CW) pump-probe SERS. By comparing with solution phase normal Raman spectra, the characteristic spectral variations observed upon 532 nm optical pumping can be attributed to an oxidation process which occurs on the surface species followed by desorption of the oxidized surface species from the gold nanoparticles. Interrogating the plasmon-driven processes over a wide range of temperatures reveals that neither process is purely driven by the thermal effects associated with the optical pumping and the apparent activation energies of both steps are estimated based on semi-quantitative SERS analysis. Our observation identifies a more detailed reaction pathway for this classic model system under considerably simplified reaction

conditions, adding to the current mechanistic background for future plasmon-driven chemistry studies and applications.

Introduction.

With a large cross-section for light-matter interactions that arises from localized surface plasmon resonance (LSPR) excitation, plasmonic materials have generated substantial interest as promising candidates for capturing, harnessing, and converting solar energy.[1-5] When illuminated with light, these materials harvest photon energy through their plasmon resonance, whose decay generates energetic hot carriers on a 1-100 fs timescale.[3, 6-9] These can be transferred to surrounding molecules or semiconductors, inducing or enhancing processes such as photovoltaic current generation,[10-11] plasmon-mediated synthesis[12-16] and photocatalysis[17-22]. Numerous examples have been reported in recent years, covering a wide range of both metal/semiconductor and metal/molecule systems.[23-25] Plasmonically generated hot electrons have been used to drive thermodynamically uphill conversions and catalyze kinetically sluggish reactions, such as CO_2 reduction into methane and other hydrocarbonates,[26-28] nitrogen fixation,[29] and the room-temperature dissociation of H_2.[20]

In addition to hot electrons, transiently unoccupied states below the Fermi level in the metal may also contribute to mediating reactions. Hot holes have been shown to be the major active species in the oxidation of citrate molecules, leading to anisotropic growth of silver nanostructures.[12, 30] With matched energetics, hot electrons and hot holes generated within the same plasmonic moiety could be simultaneously utilized to drive different reactions, allowing autonomous solar water-splitting devices, where the oxidation and reduction steps both result from hot carriers generated by the excitation of surface plasmons.[14]

As the number of successful examples rises, so does the appeal for further understanding of the chemical details and underlying mechanisms at stake, requiring sufficiently simple model reactions and experiments to allow potential intermediates to be identified and individual chemical steps to be analyzed. The redox chemistry of ferri- and ferro- hexacyanide complexes ($[Fe(III)(CN)_6]^{3-}/[Fe(II)(CN)_6]^{4-}$, abbreviated as Fe(III)/Fe(II)) constitutes a promising candidate to fulfill this role, as recent reports have demonstrated their ability to act both as electron acceptors[31-33] and hole acceptors[34-36] in plasmon-driven reactions. Moreover, ferri-/ferro hexacyanide complexes, when paired with selected hole scavengers, have been used as a model system to study the kinetics and mechanisms of plasmon-assisted multi-electron transfer reactions, such as CO_2 reduction.[37] Understanding the detailed mechanisms behind these reactions could provide new perspectives towards unconventional and economically appealing plasmonic strategies for facilitating many classic chemical processes, which is why there is a pressing need for understanding the plasmon-driven redox chemistry of the Fe(III)/Fe(II) couple in detail.

Global balance analysis, such as product yield measurements by mass spectroscopy,[22] scanning electrochemical microscopy,[34-36] and UV-Vis spectroscopy[31-33] provide irrefutable evidence of the final products of these chemical reactions at a macroscopic level, but provide limited capability for pinpointing the behavior of species within plasmonic reactive sites. In order to fully rationalize and optimize the plasmon-driven process, more fundamental insights on the catalytic mechanism which takes place in plasmonic hotspots is needed, ideally with vibrational spectroscopic methods to provide chemical signatures. Plasmon-enhanced Raman spectroscopies constitute the ideal tool for providing such information, as the Raman signal from molecules located in plasmonic hot spots is selectively enhanced, providing a chemical fingerprint of the subset of molecules which actually undergoes plasmon driven chemistry, while minimizing the influence of inert molecules. [38-40]

Our previous investigations of plasmon-driven charge transfer reactions with surface-enhanced Raman spectroscopy (SERS) have dealt with pyridine derivatives,[41-42] revealing multiple side reactions, such as isomerization and intermittent molecular hopping, and leading to unstable anion radicals as products. The complex and bifurcated nature of such reactions severely hinders our ability to assign an unambiguous chemical mechanism, which is why, in this paper, we employ continuous-wave (CW) pump-probe SERS to analyze the plasmon-driven redox chemistry of the Fe(III)/Fe(II) couple.

While studying the reaction in air or in vacuum conditions for a wide range of temperatures (10 K-356 K), we considerably simplify the reaction conditions with respect to other studies, modulating the reaction rates and eliminating the influence of other chemical species and diffusion. Indeed, we are able to unambiguously identify the different intermediate chemical species and analyze the reaction kinetics. Our results demonstrate the presence of two photochemically driven steps, and provide insight into reconciling the femtosecond time scales of plasmon decay and hot carrier generation with the observed second to minutes reaction advancement timescales.

Methods

Sample Preparation Gold nanoparticle oligomers have been synthesized which consist of aggregated 60 nm diameter gold spherical cores and potassium ferricyanide ($K_3[Fe(III)(CN)_6]$). In a typical sample preparation, the aggregation of gold nanoparticles was induced by adding 20 μL of 3 mM aqueous solution of $K_3[Fe(III)(CN)_6]$ (Sigma-Aldrich, ≥99 %) into 1mL of colloidal 60 nm diameter gold nanoparticles (0.25 mg Au/mL, STA Technologies Inc.). The gold colloid was allowed to aggregate for 50 min at room temperature. The Vis-NIR extinction spectrum for the aggregated colloidal solution was measured using a spectrophotometer in double beam mode (Cary 5000, Agilent Technologies). A 10 μL aliquot of the aggregated gold colloid was then dropcast onto a microscope glass coverslip (VWR International, No.2) and allowed to dry in air, forming layers of densely immobilized nanoparticle oligomers at high concentration on the glass substrate. Prior to using, microscope glass coverslips underwent piranha treatment (3:1 H_2SO_4:30%H_2O_2) followed by thorough rinsing with Milli-Q water. Coverslips were then immersed in a base treatment (5:1:1H_2O:NH_4OH:30%H_2O_2), sonicated for 60 min, and again thoroughly rinsed with Milli-Q water.

CW Pump-Probe SERS Measurements. CW pump-probe SERS measurements at room temperature in air were performed on a microscope setup (Nikon Ti−U) using a 40× objective (Nikon, NA = 0.60). During measurements, samples were irradiated with a spatially overlapped 785 nm CW probe laser beam (Renishaw Inc.) and a 532 nm CW pump laser beam (Spectra-Physics). The scattered radiation was then sent into an Acton spectrograph (Princeton Instruments) equipped with a PIXIS 400BR CCD Camera (Princeton Instruments). A mechanical shutter (Picard Industries) was used to precisely control the pumping time.

In environmental temperature dependence experiments (10 K-295 K), samples were placed on an Agile Temperature Stage inside the optical sample chamber of a cryostat (Cryostation S50, Montana Instruments), which was held under vacuum during the experiments. The stage surface temperature readout is taken as the environmental temperature of the system studied. A common sequence for data acquisition consisted of (1) collecting a single frame SER spectrum at 785 nm for 20 s as the initial spectrum, (2) exposing the sample to the 532 nm laser for a certain amount of time while the probe is shuttered and the camera is not acquiring spectra, then (3) collecting a second SER spectrum at 785 nm for 20 s as the final spectrum. Any possible spectral variations induced by the 785 nm laser during the data acquisition are excluded by subtracting the "probe background" from all difference spectra, which is defined as the difference between two consecutive 20 s-frames acquired with the 785 nm probe beam under a given environmental temperature (see section S5 in SI for detailed data treatment). A 100× objective (Zeiss, NA=0.9) was used to focus the 785 nm CW laser beam (Renishaw Inc.) and the 532 nm CW laser beam (M squared) onto the sample. The scattered light was then collected by the same objective and sent into a SpectraPro HRS-500 Spectrograph (Princeton Instruments) equipped with a PIXIS 400BR CCD Camera (Princeton Instruments). A mechanical shutter (Picard Industries) was used to precisely control the pumping time.

Results and Discussion

CW Pump-Probe SERS of Plasmon Driven Chemistry. As revealed by their bulk extinction spectra (Figure 1), aggregated gold colloids in solution can support multicore plasmon modes, as shown by the broad band at higher wavelengths (700-800 nm) in addition to the monomer plasmon mode of gold nanoparticles at 540 nm, indicative of forming SERS active plasmonic hot spots.[43] In the following experiments, the 532 nm beam resonant with the monomer plasmon mode is used

as an optical pump to trigger the reactions, while the processes are monitored with SERS using the 785 nm probe beam that falls within the broad multicore plasmon band to maximize the Raman enhancement factor.[44]

A representative set of pump-probe SER spectra is presented in Figure 2. First, we focus on the carbonyl/nitryl stretching spectral region (2000-2500 cm^{-1})[45]. A typical pre-pumping spectrum is shown in the bottom of Figure 2.a, consisting of two major bands at 2115 cm^{-1} and 2150 cm^{-1} with a relatively low intensity band centered at 2190 cm^{-1}, suggesting the presence of a mixture of adsorbed Fe(II) and Fe(III) surface species, the origin of which will be discussed in detail in following sections. The stability of the system under the probe beam is evaluated by collecting five SER spectra (t_{exp} = 20 s). As shown in the bottom part of the waterfall plot in Figure 2, the spectra only show small intensity fluctuations, demonstrating that the probe beam is unable to trigger the reaction on a 100 s timescale. The sample is then exposed to the 532 nm pump concurrent with the 785 nm probe for 720 s. Upon exposure to the pump an immediate and significant decrease in the intensity of the 2115 cm^{-1} and 2150 cm^{-1} bands is observed. The intensity of the 2190 cm^{-1} band increases within the first 2 frames after pumping and then gradually drops below its initial intensity, with the emergence and increase of a distinctive new band centered at 2134 cm^{-1}. Afterwards, the pump beam is shuttered and continued acquisition of SER spectra with the 785 nm probe reveals that the spectral signatures remain unchanged after pump is turned off. The rise and subsequent depletion of the 2190 cm^{-1} band suggests it to be the signature of an intermediate species, while the accompanied appearance and continued growth of the 2134 cm^{-1}

band indicate its role as a signature of the final product (within the timescale of the experiment). This can be seen clearly from the time trace of both peaks shown in Figure 2. c.

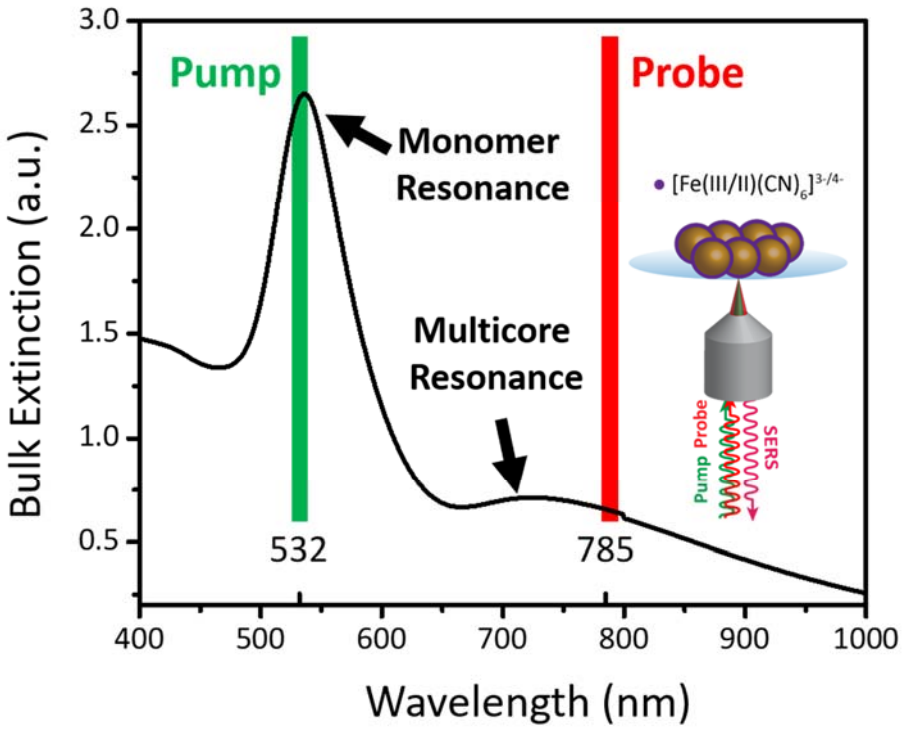

Figure 1. Visible-NIR extinction spectrum of the ferri-/ferrocyanide @ AuNP in solution phase. Inset: schematic illustration of observing plasmon-driven processes in the ferri-/ferrocyanide @ AuNP system with CW pump-probe SERS.

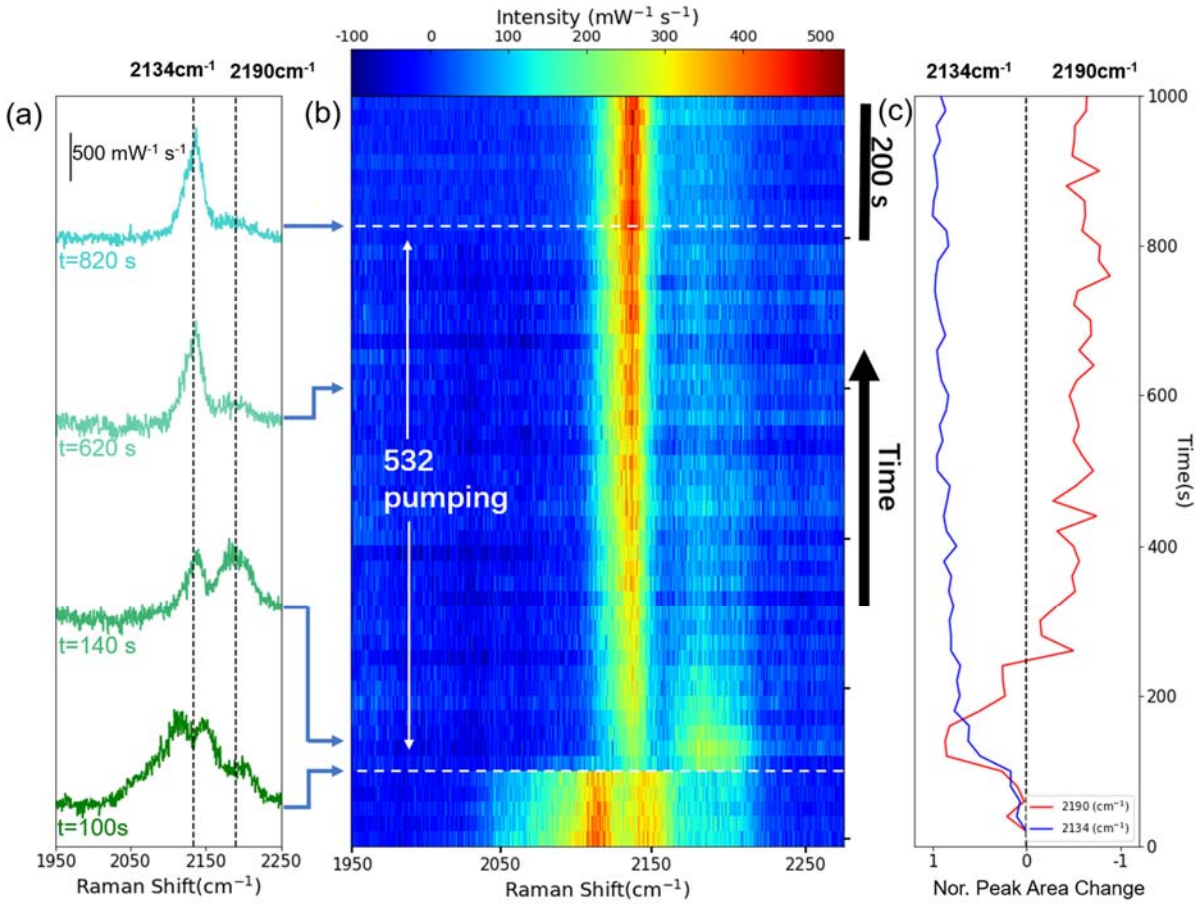

Figure 2. Representative plasmon-induced spectral variations in ferri-/ferrocyanide @ AuNP system at one spot. (a) SER spectra at t=100 s (before pumping), t=140 s, t=620 s (during pumping) and t=820 s (after pumping). Intensity unit mW^{-1} s^{-1}: camera counts divided by the laser power (mW) and acquisition time (s) used to obtain the spectrum. (b) Waterfall plot shows time-dependent SERS data recorded by 785 nm probe beam (4 μW/μm^2). Vigorous spectral changes were observed after 532 nm optical pumping (41 μW/μm^2) was turned on. (c) Time trace of changes in peak area in bands at 2190 cm^{-1} and 2134 cm^{-1}. Values of area change for both peaks are normalized to the final area change of 2134 cm^{-1} peak. (See section S1 in SI for more details).

Band Assignment and Process Identification. In order to identify the peaks, normal Raman reference spectra of saturated potassium ferricyanide and potassium ferrocyanide solutions are collected, as shown in the bottom panels of Figure 3. The solution phase Raman spectrum of Fe(II) exhibits a CN E_g vibrational mode at 2059 cm^{-1} and a CN A_{1g} vibrational mode at 2095 cm^{-1}; while

that of Fe(III) shows a major CN A_{1g} vibrational mode at 2134 cm^{-1}, with a CN E_g vibrational mode appearing as a shoulder peak at around 2129 cm^{-1}.[46] Positions of the three peaks in the initial spectrum of pump-probe SERS (Figure 3.a, top), obtained under 785 nm illumination at t=100 s prior to 532 nm pumping, are in good agreement with the two CN modes of Fe(II) and the major CN mode of Fe(III) in solution-phase normal Raman spectra, albeit with a consistent blue-shift of around 55 cm^{-1} for all CN bands. Such blue-shift of the CN stretching modes has commonly been reported as characteristic of bridging CN ligands, both within various organometallic complexes[47-49] and SERS (at the surface of plasmonic electrodes and/or nanostructures) contexts.[50-52] This indicates the formation of strongly chemisorbed cyanide complexes, in which at least one CN group bonds to the surface through the nitrogen lone pair to the second metal center, which resides in a mostly C-N antibonding orbital, increasing the strength of the carbon-nitrogen bond.[53] These experimental studies are also corroborated by theoretical analysis, as shown by Korzeniewski et al., which calculated the vibrational spectra of ferri-/ferrocyanide adsorbed on metal electrodes.[54] Specifically, their work shows that the observed blue shifts of the adsorbate are directly correlated to the bonding strength, as shown by the evaluated binding energies. The 55cm^{-1} shift observed in our work is in quantitative agreement with their predictions.

Based on comparison with reference Raman spectra, we assign the initial spectrum (Figure 3. a) to a mixture of Fe(II) and Fe(III) cyanide complexes chemisorbed on the gold surface. This observation suggests that the surface Fe(III) species undergoes spontaneous reduction on the gold surface during the aggregation process, until an equilibrium distribution of surface Fe(III)/Fe(II) is reached. A similar mixture of Fe(III) and Fe(II) species in the initial spectrum is also observed when the sample is prepared by adding $K_4[Fe(II)(CN)_6]$ solution into the colloidal gold nanoparticle solution (see section S2 in SI), confirming that the initial equilibrium Fe(III)/Fe(II)

distribution in the gold nanoparticle surface is indeed determined by the alignment of the Fermi level of the gold nanoparticle and the HOMO/LUMO orbital of the ferri-/ferrocyanide couple in the solution environment where the initial adsorption of molecules to the gold surface and the aggregation of gold nanoparticles take place. Figure 3.b shows that pumping with the 532 nm beam leads to the disappearance of $(Fe(II)\text{-}CN)_{ads}$ band and the increase of $(Fe(III)\text{-}CN)_{ads}$ band, indicating that surface Fe(II) ions chemisorbed on gold are being oxidized to Fe (III) ions. Also, the emerging band at 2134 cm^{-1} overlaps well with the major CN stretching mode of Fe(III) solution-phase normal Raman spectrum, suggesting the progressive desorption of the $(Fe(III)\text{-}CN)_{ads}$ species. After extensive pumping (Figure 3c), the conversion from the 2190 cm^{-1} $(Fe(III)\text{-}CN)_{ads}$ band to a 2134 cm^{-1} Fe(III)-CN band advances until near completion. It is noted that the intensity of the 2190 cm^{-1} band does not completely drop to zero, indicating the presence of some Fe(III) species trapped in unfavorable reaction sites which remain adsorbed to the surface.

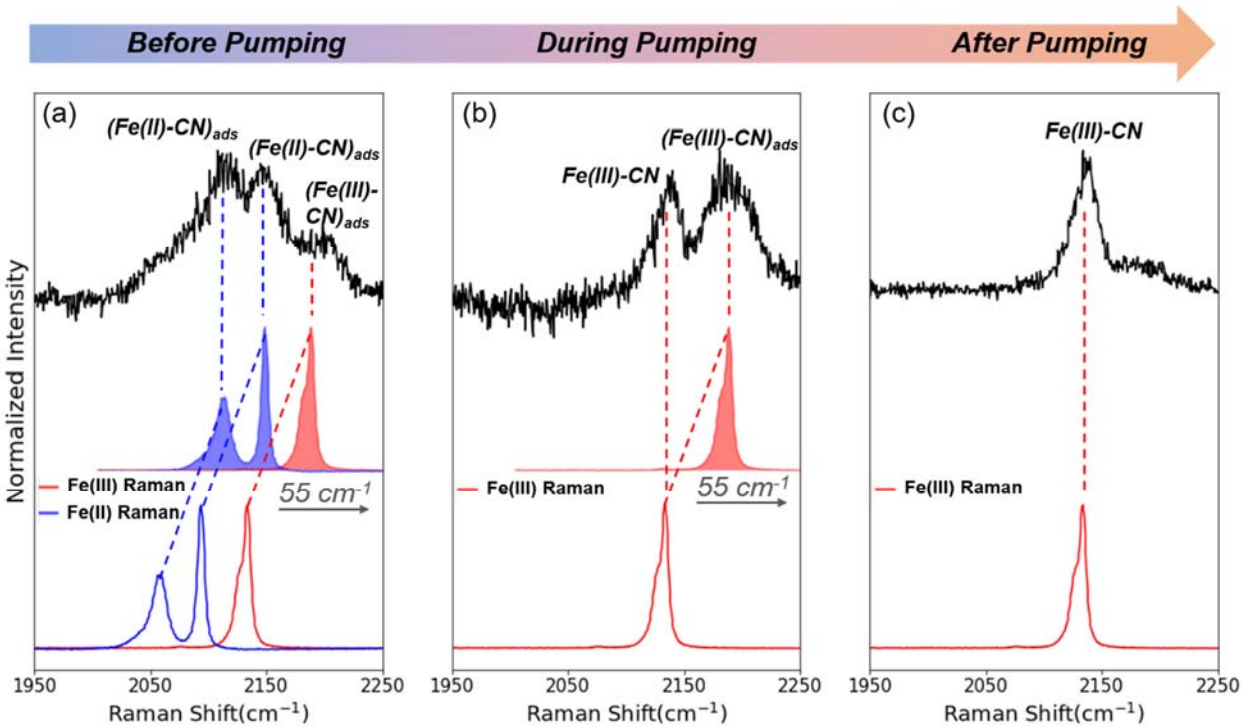

Figure 3. Comparison between solution-phase normal Raman spectra and selected CW pump-probe SER spectra before pumping (a), during pumping (b), and after pumping (c). Bottom: normal Raman spectra of saturated potassium ferricyanide (III) solution (red) and potassium ferrocyanide (II) solution (blue) using 785 nm excitation. Middle: blue-shifting the bottom spectra by 55 cm^{-1} to guide the comparison. Top: CW pump-probe SER spectra in ferri-/ferrocyanide @ AuNP system at various times, with proposed peak assignments.

While the conversion of surface $Fe(II)_{ads}$ to $Fe(III)_{ads}$ is clearly a charge transfer step, the desorption process is less clear. Electrochemical SERS experiments were conducted to support our proposed reaction pathway, in particular to show that the second step is not a redox reaction (for more details see section S3 in SI). By cycling the potential between -0.3 V and 0.5 V under SERS monitoring, it can be seen that the appearance of 2190 cm^{-1} band, corresponding to strongly adsorbed Fe(III), is not correlated to any redox event/current peak, suggesting that the conversion between the 2134 cm^{-1} peak and the 2190 cm^{-1} peak is not associated with any charge transfer step in the Fe(II)/Fe(III) redox reaction.

Furthermore, since the desorption of surface $Fe(III)_{ads}$ species requires the breaking of bridging CN bonds with the gold surface, we looked at plasmon-induced spectral variations in the low wavenumber region to support that the second step indeed corresponds to the desorption of surface species. The adsorption of molecules to substrates is usually accompanied by a Raman peak shift and the appearance of extra Raman peaks in the low wavenumber (100-600 cm^{-1}) region due to the adsorption and/or bonding to the substrate.[51-52, 55]. Indeed, the low wavenumber spectrum collected prior to the 532 nm pumping differs from the normal Raman spectrum of $K_3[Fe(III)(CN)_6]$ solution, featuring the shifted δ(FeCN) bending mode at 530 cm^{-1} and a new peak at 275 cm^{-1} which can be assigned to ν(Au-N) (See section S4 in SI).[50, 52, 56-57] These vibrational signatures support the idea that the initial species are strongly adsorbed and form a surface bond with the gold nanoparticles.

The two spectral windows (between 250 cm^{-1} and 2300 cm^{-1}) are covered with reasonable spectral resolution by shuttering the 532 nm laser after each pump step, and using the 785 nm probe beam to sequentially acquire a low wavenumber region spectrum and a high wavenumber region spectrum. To highlight the net changes induced by optical pumping, the difference spectra (we subtract the spectrum right before pumping start) are shown in Figure 4. As expected, pumping the sample with the 532 nm laser induces changes in the low wavenumber region correlated to the spectral variations in the 2000-2300 cm^{-1} region discussed in the previous section. The 275 cm^{-1} and 530 cm^{-1} peak intensities decrease at the same pace as the accumulation of final product, characterized by the 2134cm^{-1} peak, supporting the idea that the optical pump induces reconfiguration of the intermediate species, leading to an inert final product which is not in strong interaction with the surface. Comparison with the normal Raman of $K_3[Fe(III)(CN)_6]$ solution conclusively reveals the identity of the final species, confirming our preliminary band assignment.

Therefore, our experimental evidence collectively suggest the observation of plasmon-driven processes in ferri-/ferrocyanide gold nanoparticle oligomers consisting of two steps: a charge transfer step between gold nanoparticles and surface Fe(II) species followed by desorption of the surface Fe(III) species. Noteworthy, in our study we only probe a small fraction of the total surface – the plasmonic hotspots, and therefore even substances present in trace amounts in the surroundings could potentially act as the final electron scavenger, completing the charge flow cycle. Other reports in the literature describe surface accumulation of photogenerated electrons resulting from the transfer of hot-holes to the adsorbates.[58] Moreover, the charge buffer character of plasmonic nanoparticles has been extensively demonstrated experimentally, and can be stable for up to several minutes,[59] which is the key in plasmon-driven multielectron transfer processes, as recently pointed out in the literature.[33] These studies suggest that in our system, gold nanoparticles serve as an electron reservoir to temporarily capture the excess hot electrons generated during the reaction, which are eventually transferred to electron acceptors present in trace amounts, such as residual water.

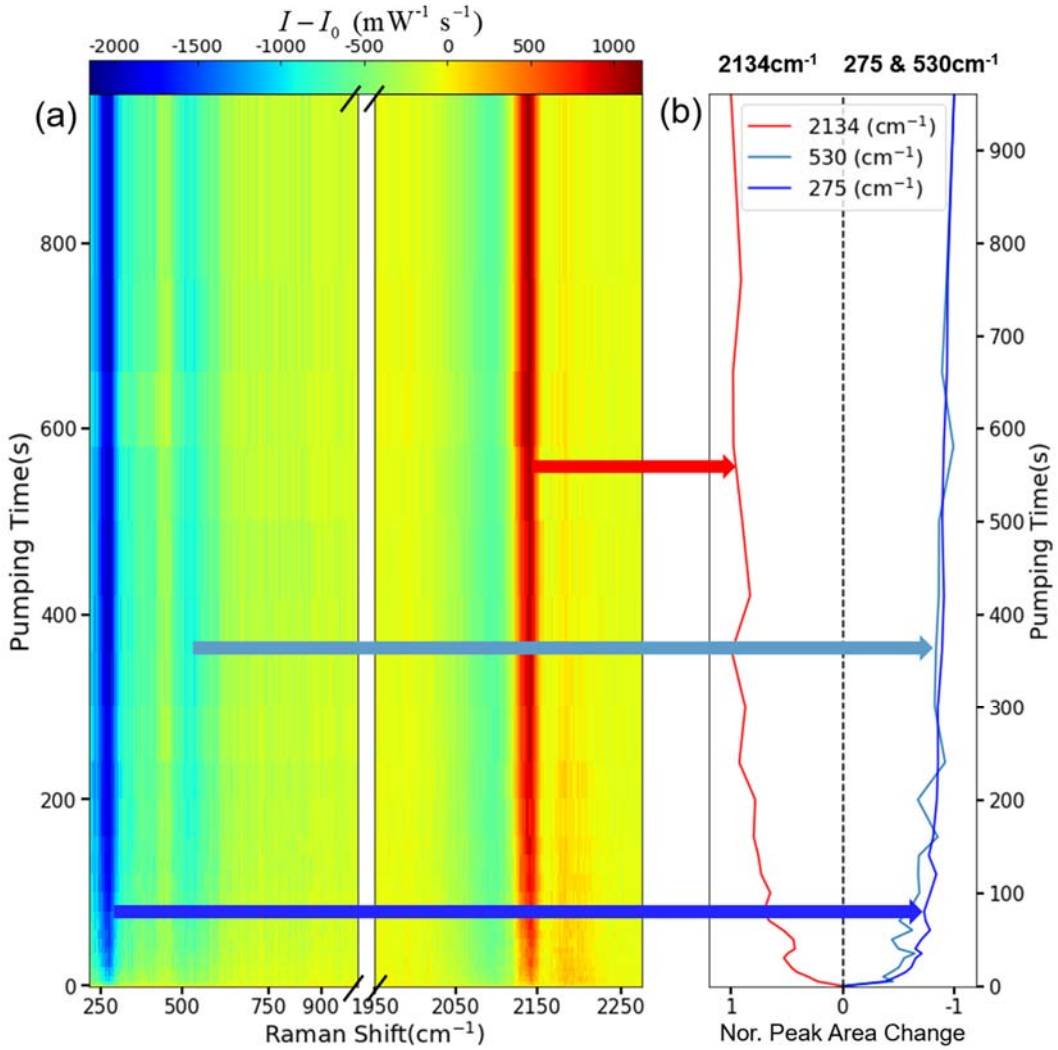

Figure 4. Correlated intensity decreases in low-frequency peaks (275 cm^{-1} and 530 cm^{-1}) and intensity increase in free Fe(III)-CN peak (2134 cm^{-1}) under 532 nm optical pumping in ferri-/ferrocyanide @ AuNP system. (a) Waterfall plot shows the evolution of spectral variations highlighted by difference SER spectra. All SERS data are recorded by 785 nm probe beam (4 μW/μm^2) at room temperature. 532 nm laser (41 μW/μm^2) was used as the optical pump. Pumping time refers to the accumulated total pumping time. Intensity unit mW^{-1} s^{-1}: camera counts divided by the laser power (mW) and acquisition time (s) used to obtain the spectrum. (b) Time trace of changes in peak area in 275 cm^{-1}, 530 cm^{-1} and 2134 cm^{-1} bands. The absolute value of area change in each peak is normalized to one.

Environmental Temperature Influence. With the observed bands assigned, we next focused on understanding the influence of temperature in the plasmon-driven processes and its implications

on the nature of each plasmon-driven step. In short, two classes of plasmon-mediated processes can operate to trigger and/or enhance chemical reactions: (i) through hot-carrier transfer, which results in charge transfer processes and chemical reactions that involve bond formation and breaking; (ii) through plasmonic heating, where the heat generated during the plasmon decay and hot carrier relaxation by electron-phonon and phonon-phonon coupling serves to accelerate or initiate the reaction.[60] A lot of effort from the community has been directed towards understanding which one of these two mechanisms operates or dominates each plasmon-driven process. In order to gather mechanistic insight, we proceeded to study the reaction over a wide range of different environmental temperatures.

Difference spectra are shown in Figure 5, where each data point represents the average over at least 3 spots to minimize the influence of sample aggregation heterogeneity among different spots. Figure 5.a shows a series of difference spectra resulting from pumping the sample for a fixed time (t_{pump} = 40 s) at different environmental temperatures while keeping the pumping power constant (P =264 μW/μm^2). All datasets show the same, previously observed, tendency: the depletion of surface Fe(II) species leads to a negative feature in the difference spectra to the left of 2115 cm^{-1} and another negative feature at around 2150 cm^{-1} , while the positive feature around 2190 cm^{-1} accounts for the increase of adsorbed Fe(III) species. The feature centered at 2134 cm^{-1} comes from the formation of free Fe(III) species as the final product. The overall trend clearly suggests that higher environmental temperatures (from 200 K to 295 K) accelerate the reaction, resulting in more final product being generated with a fixed pumping time and power. Noteworthy, the reaction happens even at temperatures as low as 10 K (see section S6 in SI for a detailed dataset), albeit slowly.

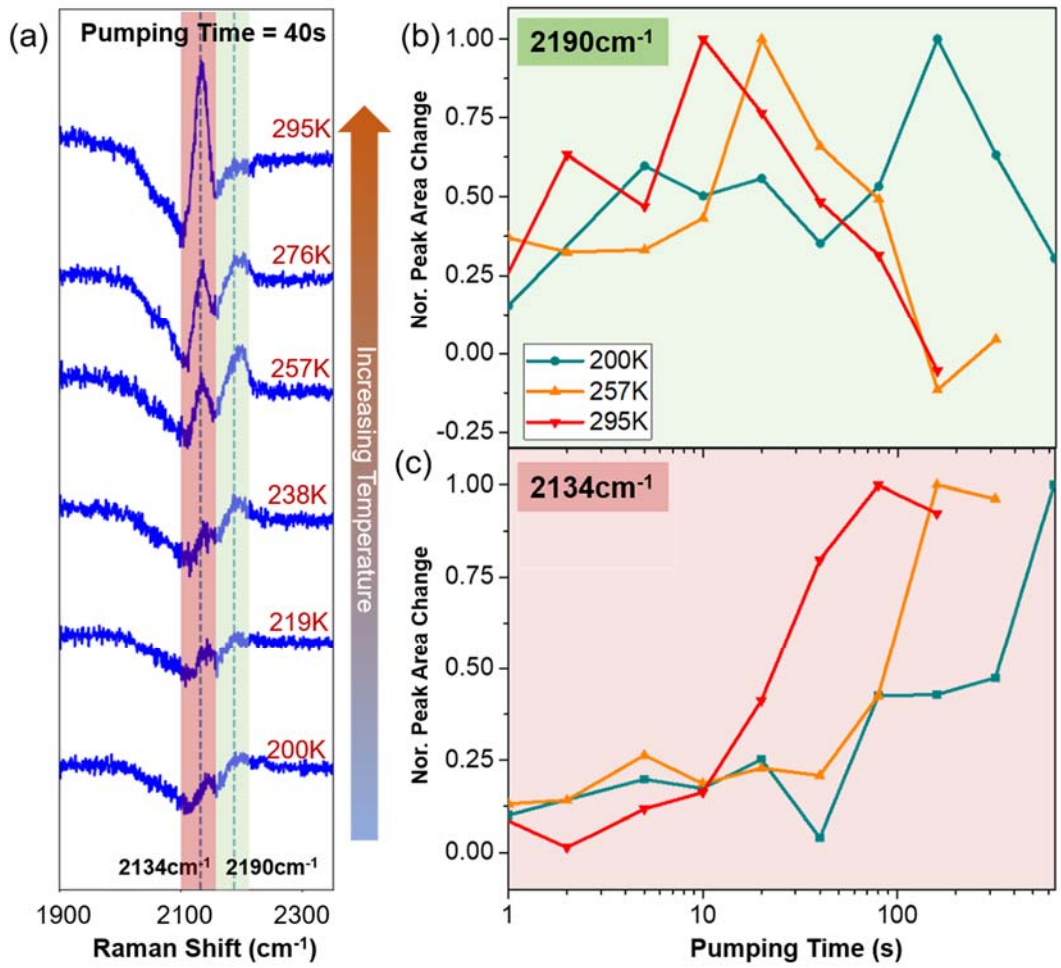

Figure 5. Environmental temperature dependence of plasmon-driven processes in ferri-/ferrocyanide @ AuNP system. (a) Difference SER spectra at various environmental temperatures with fixed pumping time (40 s) and pumping power (264 μW/μm^2). (b), (c) Time traces of changes in peak area under different environmental temperatures in 2190 cm^{-1} peak and 2134 cm^{-1} peak, respectively, with fixed pumping power at 350 μW. The absolute value of area change in each peak is normalized to one. For all measurements presented in this figure, 532 nm laser beam was used as the optical pump while 785 nm laser beam (18 μW/μm^2) was used to record SER spectra. Each difference spectrum/data point is averaged over repetitive measurements on at least 3 spots to account for the aggregation heterogeneity.

In order to gather kinetic information, we selected a temperature range (from 200 K to 295 K) in which the reaction can be driven to near completion within reasonable reaction times. The

reaction kinetic time traces of 2190 cm^{-1} and 2134 cm^{-1} under three different temperatures are constructed by quantifying the conversion for various pumping durations, as is shown in Figure 5. (b, c). At higher temperature, the intermediate peak at 2190 cm^{-1} maximizes and declines within a shorter period of time, with the final product peak at 2134 cm^{-1} grows in at a faster rate. The kinetic time traces clearly demonstrate that both the oxidation and desorption processes are positively related to the environmental temperature. To further understand the temperature-dependent kinetics, the two processes are modeled as a consecutive reaction and Arrhenius analysis is performed to calculate apparent activation energies for both steps using the rate constants extracted from the time traces in Figure 5 (see section S8 in SI for details). The apparent activation energy is calculated to be 16 kJ mol^{-1} and 13 kJ mol^{-1} for the oxidation step and the desorption step under laser illumination, respectively. These activation energies are similar to the reported activation free energies in plasmon-driven charge transfer reactions between gold nanoparticles and ferri-/ferrocyanide redox couple in the literature.[32]

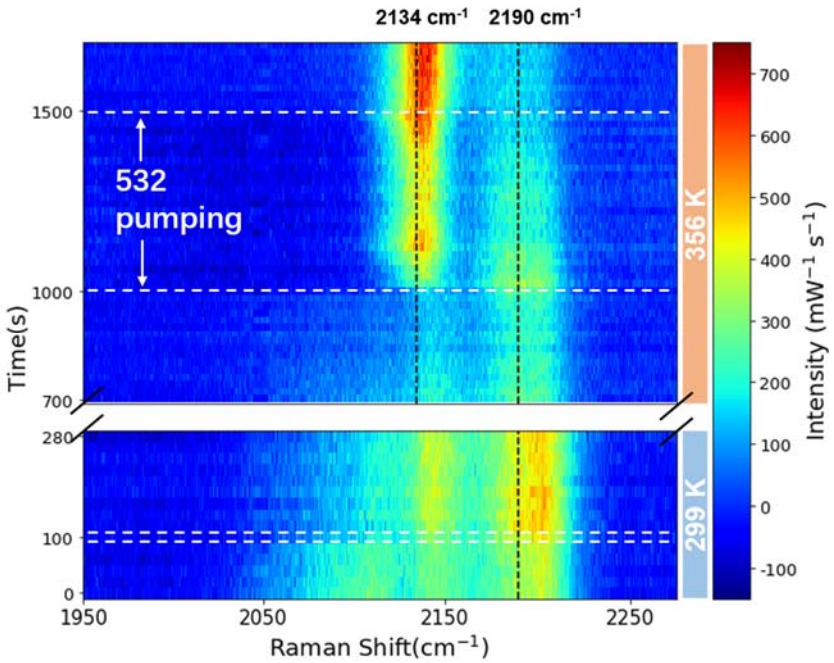

Figure 6. Waterfall plot shows the SERS data recorded by 785 nm probe (4 μW/μm^2) under the influence of optical pumping and/or environmental heating. During the experiment, the sample was first held at room temperature for 100 s and then irradiated by 532 nm pump beam (4 μW/μm^2) for 20 s. The sample was heated to 356 K during the course from t=280 s through t=700 s. Data acquisition was resumed after the set temperature was reached and stabilized. After holding the sample at 356 K for 300 s, the 532 nm pump (41 μW/μm^2) was let in again for 500 s and then shut off. The drop of the overall intensity after the heating process is because of the loss of focus due to the thermal expansion of the setup. Intensity unit mW^{-1} s^{-1}: camera counts divided by the laser power (mW) and acquisition time (s) used to obtain the spectrum.

Keeping in mind that the local temperature at the hotspots might differ from the environmental temperature of the bulk medium due to photo/plasmon-induced heating,[22, 35, 61-62] we tried to drive the reaction by heating the sample, as a control experiment. A heating stage is used to heat up the sample under SERS monitoring to investigate whether either of the two observed reaction steps could be purely thermally driven. Previously, our group has used Stokes/Anti-Stokes Raman thermometry to establish a higher bound on the temperature achieved for samples prepared in the

same manner as this work. At the maximal pump power used here, such limit is found to be 350 K.[63] Taking this as reference, a freshly prepared sample is heated to 356 K and the equilibrium temperature was held for as long as 1000 s. No substantial spectral variations are observed by 785 nm Raman probe except for a slow and gradual decrease in the overall intensity due to mild sample degradation and/or thermal drift, showing that the first step cannot be purely thermally driven (see section S7 in SI). In order to investigate how the second step is related to environmental heating, we first irradiate the sample with 532 nm pump beam for 20 s under room temperature, which is sufficient to generate the intermediate, but not long enough to lead to the final product as observed previously. The pump is then blocked and the sample heated to 356 K. As can be seen in Figure 6, holding the sample at the 356 K does not trigger the second step of the reaction even after 300 s, while subsequent irradiation from the 532 nm pump (starting at t=1000 s) immediately induces a slight rise at 2190 cm^{-1} followed by a fall of the 2190 cm^{-1} band accompanied by continued increase of 2134 cm^{-1} peak.

These experiments unequivocally show that heating is not the main mechanism behind the plasmon-driven processes in the ferri-ferrocyanide/gold nanoparticle oligomer system under our experimental conditions, and shows that the reactions happen as a consequence of the presence of hot-carriers. Interestingly, in plasmonic systems, the dynamics of hot-carrier generation and transmission is known to proceed under femto-to-picoseconds time scale,[3, 7] while our observations reveal a plasmon-driven oxidation reaction on the seconds and even minutes time scale, consistent with previous plasmon-driven chemistry reports.[41-42, 64-65]. Furthermore, the experiments are performed in air or under vacuum with SERS directly monitoring the reactive hot spots, therefore the observed slow kinetics cannot be due to the diffusion of products into the detection region or due to the limited sensitivity of bulk measurements. In this way, reconciling the relatively slow

plasmon-induced oxidation process with the ultrafast nature of hot-carrier dynamics in this system requires addressing other processes which are inherent to plasmonic/molecular systems and run concurrently with the hot-hole transmission. Here, our proposed mechanism highlights the influence of the competitive reverse reaction: the hot-electron transfer from gold to Fe(III). When irradiated by the 532 nm laser, electrons from the d-band of gold oligomers are excited to the sp conduction band, leaving behind energetic holes which can be transferred to the HOMO of Fe (II) species, oxidizing it to Fe (III). At the same time, the transfer of simultaneously generated hot-electrons to the LUMO of Fe (III) species will lead to the regeneration of Fe (II). Although less favored with respect to the hole transfer, as suggested experimentally by the dominance of oxidized species in the spectra we obtained and the higher reactivity of d-band carriers predicted in theoretical works,[1] the existence of the electron transfer slows down the overall accumulation of Fe(III) on the ensemble scale, which is detected by CW SERS measurements in this work. According to this mechanism the global advancement of the reaction, which we detect in CW SERS, would rather correlate to the ratio between oxidation and reduction of chemisorbed Fe(III)/Fe(II) species, instead of the absolute rate of either step, reconciling the two timescales. This hypothesis is supported by numerous studies in which both plasmon-driven reduction and oxidation of Fe(II)/(III)$(CN)_6$ have reported to take place on the surface depending on the chemical environment of the gold nanoparticles and the existence of excess electron or hole scavengers. [22, 31-34, 36] In our case, neither strong electron donors nor acceptors are present, and the main electron/hole acceptors present are Fe(III)/Fe(II) species. This reduces the overall efficiency of the hot-hole transfer. The observed time scales are therefore the consequence of the dynamic character of the electron transfer transition for the observed species. Although not a definitive proof, our observations provide insight into a riddle that has been puzzling ultrafast plasmon-driven

chemistry studies, namely why some reactions seem difficult to trigger with short (but intense) pulses.[6, 66] Based on our observations, we speculate the reaction kinetics to be slowed down by a factor proportional to the duty cycle of the pulsed laser, when compared to CW experiments. We are currently conducting investigations with pulsed lasers to confirm such ideas, which will be object of future studies.

Similar to the oxidation process, our data shows that the breaking of the bridging bond between CN and the gold surface, and the consequential desorption of the chemisorbed Fe(III), is not purely driven by the thermal effects associated with the 532 nm optical pumping. The fact that the desorption process is only observed for the $Fe(III)_{ads}$ species suggests that the 532 nm laser is able to directly excite a transition specific to $Fe(III)_{ads}$. Aqueous Fe(III) solutions display a ligand-to-metal charge transfer (LMCT) transition at around 417 nm which is not present for Fe(II) due to the occupancy of the t_{2g} orbital.[67] These observations suggest that the interaction of the iron complex with gold leads to a decrease in the energy gap for this LMCT transition, rendering it excitable by 532 nm radiation. The excitation of LMCT transition would result in a transient decrease in the electron density on the CN ligands, weakening and breaking the bond between CN and gold and favoring desorption.

Conclusion

We have used SERS to directly observe the two step plasmon-driven reaction between ferricyanide and ferrocyanide ions within SERS active hot spots formed by gold nanoparticle oligomers. The plasmon-induced oxidation of chemisorbed Fe(II) into Fe(III) is followed by the desorption of surface Fe(III) species. The vibrational signatures of the reactants, intermediates and final product are rigorously assigned, allowing the plasmon-driven processes to be fully

rationalized and characterized. While the rate of both processes is demonstrated to increase with environmental temperature, neither step is purely driven by the local heating associated with the 532 nm optical pumping, as is shown by examining the reactions under various environmental temperatures. In light of the observed phenomena and their timescales, we propose a dynamical picture of the plasmon driven charge transfer process in which femtosecond timescale hot electron and hot hole transfer occur competitively under 532 nm illumination, leading to significantly slower macroscopic accumulation of the oxidized species and the slow chemical dynamics observed in this plasmon-induced charge transfer process.

ASSOCIATED CONTENT

Supporting Information.

The Supporting Information is available free of charge on the ACS Publications website at DOI:XXX.

Experimental details including additional SERS data and analysis.

AUTHOR INFORMATION

[†]Deceased July 28, 2019.

Corresponding Authors

*G. C. S: g-schatz@northwestern.edu.

*M. R. W. m-wasielewski@northwestern.edu

ORCID

Vitor Brasiliense: 0000-0002-5515-2218

George C. Schatz: 0000-0001-5837-4740

Michael R. Wasielewski: 0000-0003-2920-5440

Richard P. Van Duyne: 0000-0001-8861-2228

Notes

The authors declare no competing financial interest.

ACKNOWLEDGMENTS

The authors acknowledge financial support from the National Science Foundation Center for Chemical Innovation dedicated to Chemistry at the Space Time Limit (CaSTL) Grant CHE-1414466, the Air Force Office of Scientific Research MURI (FA9550-14-1-0003), NSF Grant CHE-1807278, and the Department of Defense Vannevar Bush Faculty Fellowship program (N00014-17-1-3024) for experimental studies and NSF Grant CHE-1760537 for theory.

REFERENCES

1. Christopher, P.; Moskovits, M., Hot charge carrier transmission from plasmonic nanostructures. *Annu. Rev. Phys. Chem.* **2017,** *68*, 379-398.
2. Linic, S.; Christopher, P.; Ingram, D. B., Plasmonic-metal nanostructures for efficient conversion of solar to chemical energy. *Nat Mater* **2011,** *10*, 911.
3. Brongersma, M. L.; Halas, N. J.; Nordlander, P., Plasmon-induced hot carrier science and technology. *Nat Nanotechnol* **2015,** *10* (1), 25.
4. Zhan, C.; Chen, X.-J.; Yi, J.; Li, J.-F.; Wu, D.-Y.; Tian, Z.-Q., From plasmon-enhanced molecular spectroscopy to plasmon-mediated chemical reactions. *Nature Reviews Chemistry* **2018**, 1.
5. Thomann, I.; Pinaud, B. A.; Chen, Z.; Clemens, B. M.; Jaramillo, T. F.; Brongersma, M. L., Plasmon Enhanced Solar-to-Fuel Energy Conversion. *Nano Lett.* **2011,** *11* (8), 3440-3446.
6. Brandt, N. C.; Keller, E. L.; Frontiera, R. R., Ultrafast surface-enhanced Raman probing of the role of hot electrons in plasmon-driven Chemistry. *J Phys Chem Lett* **2016,** *7* (16), 3179-3185.
7. Hartland, G. V.; Besteiro, L. V.; Johns, P.; Govorov, A. O., What's so hot about electrons in metal nanoparticles? *ACS Energy Letters* **2017,** *2* (7), 1641-1653.
8. Brown, A. M.; Sundararaman, R.; Narang, P.; Goddard III, W. A.; Atwater, H. A., Nonradiative plasmon decay and hot carrier dynamics: effects of phonons, surfaces, and geometry. *ACS Nano* **2015,** *10* (1), 957-966.
9. Ding, Q.; Shi, Y.; Chen, M.; Li, H.; Yang, X.; Qu, Y.; Liang, W.; Sun, M., Ultrafast Dynamics of Plasmon-Exciton Interaction of Ag Nanowire- Graphene Hybrids for Surface Catalytic Reactions. *Sci Rep* **2016,** *6* (1), 32724.

10. Clavero, C., Plasmon-induced hot-electron generation at nanoparticle/metal-oxide interfaces for photovoltaic and photocatalytic devices. *Nat Photonics* **2014,** *8*, 95.
11. Wu, K.; Chen, J.; McBride, J. R.; Lian, T., Efficient hot-electron transfer by a plasmon-induced interfacial charge-transfer transition. *Science (80-)* **2015,** *349* (6248), 632-635.
12. Sutter, P.; Li, Y.; Argyropoulos, C.; Sutter, E., In Situ Electron Microscopy of Plasmon-Mediated Nanocrystal Synthesis. *J. Am. Chem. Soc.* **2017,** *139* (19), 6771-6776.
13. Jin, R.; Cao, Y. C.; Hao, E.; Métraux, G. S.; Schatz, G. C.; Mirkin, C. A., Controlling anisotropic nanoparticle growth through plasmon excitation. *Nature* **2003,** *425* (6957), 487.
14. Mubeen, S.; Lee, J.; Singh, N.; Krämer, S.; Stucky, G. D.; Moskovits, M., An autonomous photosynthetic device in which all charge carriers derive from surface plasmons. *Nat Nanotechnol* **2013,** *8* (4), 247.
15. Nguyen, V.-Q.; Ai, Y.; Martin, P.; Lacroix, J.-C., Plasmon-induced nanolocalized reduction of diazonium salts. *ACS Omega* **2017,** *2* (5), 1947-1955.
16. Lee, S. J.; Piorek, B. D.; Meinhart, C. D.; Moskovits, M., Photoreduction at a Distance: Facile, Nonlocal Photoreduction of Ag Ions in Solution by Plasmon-Mediated Photoemitted Electrons. *Nano Lett.* **2010,** *10* (4), 1329-1334.
17. Zheng, Z.; Tachikawa, T.; Majima, T., Plasmon-Enhanced Formic Acid Dehydrogenation Using Anisotropic Pd–Au Nanorods Studied at the Single-Particle Level. *J. Am. Chem. Soc.* **2015,** *137* (2), 948-957.
18. Christopher, P.; Xin, H.; Linic, S., Visible-light-enhanced catalytic oxidation reactions on plasmonic silver nanostructures. *Nat Chem* **2011,** *3*, 467.
19. Christopher, P.; Xin, H.; Marimuthu, A.; Linic, S., Singular characteristics and unique chemical bond activation mechanisms of photocatalytic reactions on plasmonic nanostructures. *Nat Mater* **2012,** *11* (12), 1044.
20. Mukherjee, S.; Libisch, F.; Large, N.; Neumann, O.; Brown, L. V.; Cheng, J.; Lassiter, J. B.; Carter, E. A.; Nordlander, P.; Halas, N. J., Hot electrons do the impossible: plasmon-induced dissociation of H2 on Au. *Nano Lett.* **2012,** *13* (1), 240-247.
21. Lee, J.; Mubeen, S.; Ji, X.; Stucky, G. D.; Moskovits, M., Plasmonic Photoanodes for Solar Water Splitting with Visible Light. *Nano Lett.* **2012,** *12* (9), 5014-5019.
22. Zhou, L.; Swearer, D. F.; Zhang, C.; Robatjazi, H.; Zhao, H.; Henderson, L.; Dong, L.; Christopher, P.; Carter, E. A.; Nordlander, P.; Halas, N. J., Quantifying hot carrier and thermal contributions in plasmonic photocatalysis. *Science (80-)* **2018,** *362* (6410), 69-72.
23. Zhou, L.; Martirez, J. M. P.; Finzel, J.; Zhang, C.; Swearer, D. F.; Tian, S.; Robatjazi, H.; Lou, M.; Dong, L.; Henderson, L.; Christopher, P.; Carter, E. A.; Nordlander, P.; Halas, N. J., Light-driven methane dry reforming with single atomic site antenna-reactor plasmonic photocatalysts. *Nature Energy* **2020,** *5* (1), 61-70.
24. Jung, H.; Song, J.; Lee, S.; Lee, Y. W.; Wi, D. H.; Goo, B. S.; Han, S. W., Hierarchical metal–semiconductor–graphene ternary heteronanostructures for plasmon-enhanced wide-range visible-light photocatalysis. *J. Mater. Chem. A* **2019,** *7* (26), 15831-15840.
25. Yu, S.; Jain, P. K., Plasmonic photosynthesis of C1–C3 hydrocarbons from carbon dioxide assisted by an ionic liquid. *Nat Commun* **2019,** *10* (1), 2022.
26. Neaţu, Ş.; Maciá-Agulló, J. A.; Concepción, P.; Garcia, H., Gold–Copper Nanoalloys Supported on TiO2 as Photocatalysts for CO2 Reduction by Water. *J. Am. Chem. Soc.* **2014,** *136* (45), 15969-15976.
27. Kumari, G.; Zhang, X.; Devasia, D.; Heo, J.; Jain, P. K., Watching Visible Light-Driven CO2 Reduction on a Plasmonic Nanoparticle Catalyst. *ACS Nano* **2018,** *12* (8), 8330-8340.

28. Yu, S.; Wilson, A. J.; Heo, J.; Jain, P. K., Plasmonic control of multi-electron transfer and C–C coupling in visible-light-driven CO2 reduction on Au nanoparticles. *Nano Lett.* **2018,** *18* (4), 2189-2194.
29. Oshikiri, T.; Ueno, K.; Misawa, H., Plasmon-Induced Ammonia Synthesis through Nitrogen Photofixation with Visible Light Irradiation. *Angew. Chem. Int. Ed.* **2014,** *53* (37), 9802-9805.
30. Thrall, E. S.; Preska Steinberg, A.; Wu, X.; Brus, L. E., The Role of Photon Energy and Semiconductor Substrate in the Plasmon-Mediated Photooxidation of Citrate by Silver Nanoparticles. *J. Phys. Chem. C* **2013,** *117* (49), 26238-26247.
31. Kim, Y.; Dumett Torres, D.; Jain, P. K., Activation energies of plasmonic catalysts. *Nano Lett.* **2016,** *16* (5), 3399-3407.
32. Kim, Y.; Wilson, A. J.; Jain, P. K., The Nature of Plasmonically Assisted Hot-Electron Transfer in a Donor–Bridge–Acceptor Complex. *ACS Catal* **2017,** *7* (7), 4360-4365.
33. Kim, Y.; Smith, J. G.; Jain, P. K., Harvesting multiple electron–hole pairs generated through plasmonic excitation of Au nanoparticles. *Nat Chem* **2018,** *10* (7), 763.
34. Yu, Y.; Sundaresan, V.; Willets, K. A., Hot Carriers versus Thermal Effects: Resolving the Enhancement Mechanisms for Plasmon-Mediated Photoelectrochemical Reactions. *J. Phys. Chem. C* **2018,** *122* (9), 5040-5048.
35. Yu, Y.; Williams, J. D.; Willets, K. A., Quantifying photothermal heating at plasmonic nanoparticles by scanning electrochemical microscopy. *Faraday Discuss.* **2018,** *210* (0), 29-39.
36. Yu, Y.; Wijesekara, K. D.; Xi, X.; Willets, K. A., Quantifying Wavelength-Dependent Plasmonic Hot Carrier Energy Distributions at Metal/Semiconductor Interfaces. *ACS Nano* **2019,** *13* (3), 3629-3637.
37. Kim, Y.; Smith, J. G.; Jain, P. K., Harvesting multiple electron–hole pairs generated through plasmonic excitation of Au nanoparticles. *Nat Chem* **2018,** *10* (7), 763-769.
38. Masango, S. S.; Hackler, R. A.; Large, N.; Henry, A.-I.; McAnally, M. O.; Schatz, G. C.; Stair, P. C.; Van Duyne, R. P., High-Resolution Distance Dependence Study of Surface-Enhanced Raman Scattering Enabled by Atomic Layer Deposition. *Nano Lett.* **2016,** *16* (7), 4251-4259.
39. Li, C.-Y.; Le, J.-B.; Wang, Y.-H.; Chen, S.; Yang, Z.-L.; Li, J.-F.; Cheng, J.; Tian, Z.-Q., In situ probing electrified interfacial water structures at atomically flat surfaces. *Nat Mater* **2019,** *18* (7), 697-701.
40. Yin, H.; Lan, J.-G.; Goubert, G.; Wang, Y.-H.; Li, J.-F.; Zenobi, R., Nanoscale Surface Redox Chemistry Triggered by Plasmon-Generated Hot Carriers. *Small* **2019,** *15* (47), 1903674.
41. Sprague-Klein, E. A.; Negru, B.; Madison, L. R.; Coste, S. C.; Rugg, B. K.; Felts, A. M.; McAnally, M. O.; Banik, M.; Apkarian, V. A.; Wasielewski, M. R.; Ratner, M. A.; Seideman, T.; Schatz, G. C.; Van Duyne, R. P., Photoinduced Plasmon-Driven Chemistry in trans-1,2-Bis(4-pyridyl)ethylene Gold Nanosphere Oligomers. *J Am Chem Soc* **2018,** *140* (33), 10583-10592.
42. Sprague-Klein, E. A.; McAnally, M. O.; Zhdanov, D. V.; Zrimsek, A. B.; Apkarian, V. A.; Seideman, T.; Schatz, G. C.; Van Duyne, R. P., Observation of Single Molecule Plasmon-Driven Electron Transfer in Isotopically Edited 4, 4′ -Bipyridine Gold Nanosphere Oligomers. *J. Am. Chem. Soc.* **2017,** *139* (42), 15212-15221.
43. Negru, B.; McAnally, M. O.; Mayhew, H. E.; Ueltschi, T. W.; Peng, L.; Sprague-Klein, E. A.; Schatz, G. C.; Van Duyne, R. P., Fabrication of Gold Nanosphere Oligomers for Surface-

Enhanced Femtosecond Stimulated Raman Spectroscopy. *J. Phys. Chem. C* **2017,** *121* (48), 27004-27008.
44. Kleinman, S. L.; Sharma, B.; Blaber, M. G.; Henry, A.-I.; Valley, N.; Freeman, R. G.; Natan, M. J.; Schatz, G. C.; Van Duyne, R. P., Structure Enhancement Factor Relationships in Single Gold Nanoantennas by Surface-Enhanced Raman Excitation Spectroscopy. *J. Am. Chem. Soc.* **2013,** *135* (1), 301-308.
45. Nakamoto, K., Infrared and R aman Spectra of Inorganic and Coordination Compounds. *Handbook of Vibrational Spectroscopy* **2006**.
46. Samain, L.; Gilbert, B.; Grandjean, F.; Long, G. J.; Strivay, D., Redox reactions in Prussian blue containing paint layers as a result of light exposure. *J. Anal. At. Spectrom.* **2013,** *28* (4), 524-535.
47. Kettle, S. F. A.; Diana, E.; Boccaleri, E.; Stanghellini, P. L., The Vibrational Spectra of the Cyanide Ligand Revisited. Bridging Cyanides. *Inorg. Chem.* **2007,** *46* (7), 2409-2416.
48. Dunbar, K. R.; Heintz, R. A., Chemistry of transition metal cyanide compounds: Modern perspectives. *Prog. Inorg. Chem.* **1997,** *45*, 283-392.
49. Scott, M. J.; Holm, R. H., Molecular Assemblies Containing Linear and Bent [FeIII-CN-CuII] Bridge Units: Synthesis, Structures, and Relevance to Cyanide-Inhibited Heme-Copper Oxidases. *J. Am. Chem. Soc.* **1994,** *116* (25), 11357-11367.
50. Lowry, R., SERS and Fourier transform SERS studies of the hexacyanoferrate (III) - hexacyanoferrate (II) couple on gold electrode surfaces. *Journal of Raman spectroscopy* **1991,** *22* (12), 805-809.
51. Allen, C. S.; Van Duyne, R. P., Molecular generality of surface-enhanced Raman spectroscopy (SERS). A detailed investigation of the hexacyanoruthenate ion adsorbed on silver and copper electrodes. *J. Am. Chem. Soc.* **1981,** *103* (25), 7497-7501.
52. Loo, B. H.; Lee, Y. G.; Liang, E. J.; Kiefer, W., Surface-enhanced Raman scattering from ferrocyanide and ferricyanide ions adsorbed on silver and copper colloids. *Chem. Phys. Lett.* **1998,** *297* (1), 83-89.
53. Hanusa, T. P.; Burkey, D. J. Cyanide Complexes of the Transition Metals. In *Encyclopedia of Inorganic Chemistry*; King, R. B., Ed.; Wiley: Oxford, 1994; Vol. 2, pp 943−949.
54. Korzeniewski, C.; Severson, M. W.; Schmidt, P. P.; Pons, S.; Fleischmann, M., Theoretical analysis of the vibrational spectra of ferricyanide and ferrocyanide adsorbed on metal electrodes. *J Phys Chem* **1987,** *91* (22), 5568-5573.
55. Mažeikienė, R.; Niaura, G.; Malinauskas, A., Electrochemical redox processes at cobalt hexacyanoferrate modified electrodes: An in situ Raman spectroelectrochemical study. *J. Electroanal. Chem.* **2014,** *719*, 60-71.
56. Loo, B. H., Enhanced Raman scattering from hexacyanoferrate (II) and (III) ions adsorbed on silver electrode surfaces. *Chem. Phys. Lett.* **1993,** *213* (5), 479-484.
57. Chan, M. Y.; Leng, W.; Vikesland, P. J., Surface-Enhanced Raman Spectroscopy Characterization of Salt-Induced Aggregation of Gold Nanoparticles. *Chemphyschem* **2018,** *19* (1), 24-28.
58. Schlather, A. E.; Manjavacas, A.; Lauchner, A.; Marangoni, V. S.; DeSantis, C. J.; Nordlander, P.; Halas, N. J., Hot Hole Photoelectrochemistry on Au@SiO2@Au Nanoparticles. *J Phys Chem Lett* **2017,** *8* (9), 2060-2067.

59. Novo, C.; Funston, A. M.; Mulvaney, P., Direct observation of chemical reactions on single gold nanocrystals using surface plasmon spectroscopy. *Nat Nanotechnol* **2008,** *3* (10), 598-602.
60. Jain, P. K., Taking the Heat Off of Plasmonic Chemistry. *J. Phys. Chem. C* **2019,** *123* (40), 24347-24351.
61. Keller, E. L.; Kang, H.; Haynes, C. L.; Frontiera, R. R., Effect of Silica Supports on Plasmonic Heating of Molecular Adsorbates as Measured by Ultrafast Surface-Enhanced Raman Thermometry. *ACS Appl Mater Interfaces* **2018,** *10* (47), 40577-40584.
62. Keblinski, P.; Cahill, D. G.; Bodapati, A.; Sullivan, C. R.; Taton, T. A., Limits of localized heating by electromagnetically excited nanoparticles. *J. Appl. Phys.* **2006,** *100* (5), 054305.
63. Wu, Y.; Yang, M.; Ueltschi, T. W.; Mosquera, M. A.; Chen, Z.; Schatz, G. C.; Van Duyne, R. P., SERS Study of the Mechanism of Plasmon-Driven Hot Electron Transfer between Gold Nanoparticles and PCBM. *J. Phys. Chem. C* **2019,** *123* (49), 29908-29915.
64. Rao, V. G.; Aslam, U.; Linic, S., Chemical requirement for extracting energetic charge carriers from plasmonic metal nanoparticles to perform electron-transfer reactions. *J. Am. Chem. Soc.* **2018,** *141* (1), 643-647.
65. Brooks, J. L.; Frontiera, R. R., Competition between Reaction and Degradation Pathways in Plasmon-Driven Photochemistry. *J. Phys. Chem. C* **2016,** *120* (37), 20869-20876.
66. Keller, E. L.; Frontiera, R. R., Ultrafast Nanoscale Raman Thermometry Proves Heating Is Not a Primary Mechanism for Plasmon-Driven Photocatalysis. *ACS Nano* **2018,** *12* (6), 5848-5855.
67. Alexander, J. J.; Gray, H. B., Electronic structures of hexacyanometalate complexes. *J. Am. Chem. Soc.* **1968,** *90* (16), 4260-4271.

TOC Graphic: